ELSEVIER

Contents lists available at ScienceDirect

Journal of Alloys and Compounds

journal homepage: www.elsevier.com/locate/jalcom



Evolution of directionally freeze-cast Fe₂O₃ and Fe₂O₃+NiO green bodies during reduction and sintering to create lamellar Fe and Fe-20Ni foams



Stephen K. Wilke^{1,*}, Jacob B. Mack, Christoph Kenel, David C. Dunand

Department of Materials Science and Engineering, Northwestern University, 2220 Campus Drive, Evanston, IL 60208, USA

ARTICLE INFO

Article history: Received 16 June 2021 Received in revised form 26 July 2021 Accepted 23 August 2021 Available online 26 August 2021

Keywords: Freeze-casting Metal foams X-ray tomography Reduction Sintering

ABSTRACT

Directional freeze-casting (FC) of powder suspensions followed by freeze-drying and sintering is a versatile and scalable processing route for creating metallic foams with highly elongated pores. Because of the high propensity for oxidation of metal powders, the use of precursor oxide powders is studied here with an additional step of H₂-reduction of oxides to metal before sintering. However, the large volume shrinkage due to oxide reduction causes foam deformations, making it difficult to optimize the FC parameters to obtain a particular foam structure. We use quasi in situ X-ray microtomography to analyze the three-dimensional structural evolution of directionally freeze-cast, lamellar Fe₂O₃ and Fe₂O₃+NiO green bodies as they are reduced by H2 at 725 °C to Fe and Fe-20Ni (at%), respectively, and sintered at 900 °C. These temperature and gas conditions result in sequential reduction and sintering steps that can be individually analyzed. Foam porosity, pore width, lamellae thickness, and macroscopic shrinkage are quantified by image analysis. Oxide green body structures match typical FC relationships: porosity increases with decreasing powder content in the FC suspension, and the lamellae spacing period, or FC wavelength, decreases with increasing freezing velocity. Upon H₂-reduction, lamellae in Fe foams buckle due to mismatch stresses from spatially-inhomogeneous reduction rates, leading to anisotropic deformation. Buckling is absent in Fe-20Ni foams due to the faster reduction kinetics of Ni/NiO that lead to more spatially uniform reduction. Reduction is responsible for 73–86% of the total volumetric shrinkage, with sintering causing the remaining shrinkage, which is nearly isotropic for all foams. The observed relationships between FC parameters, green body and metal foam structure can help guide the design and optimization of metal foams for specific technological applications.

© 2021 Elsevier B.V. All rights reserved.

1. Introduction

Metallic foams have been implemented for a wide array of technological applications, including biomedical implants [1–3], filtration [4,5], heat exchangers [6,7], batteries [8], fuel cells [9], and structural applications [10]. In all these fields, the performance of the foams is linked to their architecture, which makes control of the manufacturing processes crucial to optimizing their end use. Among the various methods for creating metal foams [10–12], freeze-casting (FC) stands out as an attractive fabrication route because it offers simple and direct control over the foam morphology and is scalable

E-mail addresses: swilke@matsdev.com (S.K. Wilke), jacobmack2022@u.northwestern.edu (J.B. Mack),

kenel.christoph@gmail.com (C. Kenel), dunand@northwestern.edu (D.C. Dunand).

[10,13]. Though the term "foam" has traditionally been used for materials produced specifically via foaming (e.g., foaming a metal melt), the ordered, porous structures obtained via freeze-casting are referred to as "foams" here due to their highly porous nature and similar applications as conventionally foamed metals.

In FC, the pore morphology is first determined by the choice of powder carrier, most commonly water, which produces a lamellar foam structure templated from ice solidification. Other powder carriers give rise to alternate architectures: for example, camphene (dendritic) [14] or tert-butyl alcohol (honeycomb) [15]. A suspension is prepared using the liquid carrier and the solid powder, with additional dispersant and polymer binder to aid in suspension stabilization [16,17]. This suspension is then frozen, directionally or non-directionally. In the case of water, as ice lamellae nucleate and grow, the powder particles are pushed into the inter-lamellar spaces, forming a composite of pure ice and packed particles embedded in ice. The ice is then sublimated to obtain a lamellar, porous green body (or preform) with open pores (channels) where the ice

^{*} Corresponding author.

¹ Current address: Materials Development, Inc. 825 Chicago Ave Suite G, Evanston, IL 60202, USA.

lamellae were previously. For FC metallic or ceramic materials, the green body is typically sintered to join the particles together and provide structural stability to the foam. The foam pore fraction and size can be tuned by adjusting the powder content in the FC suspension and the solidification velocities, respectively [18–20], providing the architectural control desired for metal foam applications.

While FC has been applied extensively to ceramic and polymeric materials, preparing metal foams via FC is a relatively new advance. The propensity of metals for oxidation sometimes precludes the use of submicron powders for most metals, though FC has been successfully applied with metallic powders to produce foams of Ti [21], Ag [22], and steel [23]. Another challenge is the large density of metals (in comparison to oxides), which leads to rapid sedimentation of metal powders in suspension. An alternative fabrication route is to use an oxide precursor for the metal, producing an oxide green body, which is then reduced by H₂ at elevated temperatures and sintered. Foams of Cu, Ni, Co, W, and Fe have been created from their oxides (CuO, NiO, Co₃O₄, WO₃, Fe₂O₃, respectively) using this approach [24–30]. However, the molar volume change associated with oxide reduction to metal leads to shrinkage of the foam (e.g., the Fe molar volume ratio of Fe₂O₃/Fe is 2.14/1). The foam structural evolution during the reduction and sintering steps has not been studied beyond reporting changes in macroscopic dimensions and total porosity between the oxide green body and resulting metallic foam (e.g., Refs. [31,32]). The processing-structure knowledge gap for this final processing step makes it difficult to tailor the FC procedure to achieve a specific target for metal foam architecture (e.g., size of pores and metal lamellae), often necessitating extensive trial-anderror to refine processing parameters. Manufacturing of FC metal foams would be advanced by a better understanding of how structure changes during reduction and sintering of an oxide green body to a metallic foam.

The structural evolution of sintering (without reduction) on FC foams has been investigated for ceramic materials. Lichtner et al. [33] used optical dilatometry to observe in situ the changes in diameter and height for foams made of lanthanum strontium manganite and yttria-stabilized zirconia, which revealed anisotropy in the shrinkage behavior. Sintering shrinkage was 16% and 19% linearly along the directions perpendicular and parallel to freezing, respectively, which was attributed to the closer packing of particles along the parallel direction, leading to more complete sintering. Discrete element modeling has been used to assess the mechanisms underlying such anisotropic sintering, including anisotropic particle packing, alignment of inter-particle contacts, and particle shape [33,34]. These experimental and theoretical studies can offer insight to the reduction and sintering of FC metallic foams, but to a limited extent given that the volume contraction during reduction is much greater than that of sintering alone.

A study more closely related to reduction and sintering of porous oxide green bodies was reported by Kenel et al. [35], who used in situ synchrotron X-ray microtomography to observe the structural changes of wires, extruded from inks consisting of Fe₂O₃+NiO+MoO₃ powder blends, during reduction by H₂ and sintering. These ~200 μm wires are the structural units of 3D-printed metal scaffolds used for applications similar to those of FC foams, so the manufacturing process and volumetric shrinkage challenges are similar. Kenel et al. observed rapid reduction of Fe₂O₃ and NiO prior to sintering, except in H₂-dilute conditions for which the reduction and sintering processes overlap partially. A particle size effect was also observed: micron-sized metallic powders sintered more slowly and with much less wire shrinkage than those reduced from submicron oxide powders. While not on a FC material, this prior work demonstrates the mechanistic insights that in situ X-ray tomography can provide for reduction and sintering processes, similar to another study on structural degradation of iron-based FC foams during H₂/H₂O redox cycling [36].

In this work, we use a similar quasi *in situ* synchrotron X-ray microtomography approach to probe the processing-structure relationship for directionally FC foams of Fe₂O₃ during their reduction to Fe and sintering. We track the evolution of a foam volume (3.2 mm diameter, 1.8 mm height) to elucidate changes in foam dimensions, total porosity, lamellae thickness, pore width, and intralamellae solid density. We compare how these structural parameters evolve for foams prepared using three different freezing velocities (i.e., different initial pore sizes), three levels of powder loading in the FC suspension (i.e., different initial total porosity), and a suspension containing both Fe₂O₃ and NiO powders to produce Fe-20Ni foams. An additional benefit of this study is obtaining the three-dimensional structure of as-cast green bodies, which for FC submicron oxide powders are typically too fragile for metallographic preparation and imaging.

2. Experimental procedures

2.1. Directional freeze-casting and sample preparation

Oxide green bodies were created using a water-based freezecasting method as described previously [11,32]. First, an aqueous suspension was prepared containing α-Fe₂O₃ submicron powder (99.9%, 325 ± 130 nm, Reade Advanced Materials) and a dispersant (Zephrym PD 4974, Croda, Inc.). Suspensions contained 6, 10, or 14 vol% Fe₂O₃, all with 0.5 vol% dispersant. These suspensions were ball milled for ~48 h with zirconia milling media to break up agglomerates. Separately, polyethylene glycol binder (M_n = 3350, Sigma Aldrich) was dissolved in water and added to the oxide powder suspensions, resulting in binder content of 2 vol% in the suspension. The pH of the suspension was adjusted to 5.5-6.5 by dropwise addition of 4 M HNO₃. An additional suspension was created containing 8.44 vol% Fe₂O₃ powder and 1.56 vol% nanometric NiO powder (99.5%, 45 ± 15 nm, SkySpring Nanomaterials), which upon reduction forms Fe-20Ni (at%) foams. Suspensions were degassed under rough mechanical vacuum and then placed into an ice bath to cool them to a temperature just above 0 °C.

For directional freeze-casting, a cylindrical Teflon mold (3.6 mm ID, 19.1 mm OD, 13 mm height) was placed on a copper plate and cooled to 1 °C using a thermoelectric device underneath the plate. The setup was enclosed in polymer foam insulation to minimize heat transfer radially through the mold and encourage unidirectional solidification. A small volume of cold suspension was pipetted into the mold (~ 8 mm height of liquid), and the copper plate was cooled at an exponential rate to achieve a constant freeze front velocity (following Ref. [37], Eq. 5), ending at a final temperature of -30 °C, by which point the entire sample had solidified. Samples were prepared using freezing velocities of 8, 12, or 16 µm s⁻¹. Frozen samples were pushed out of the mold, and the bottom portion of each sample (4-5 mm) was cut with a razor blade to (i) remove any sedimentation layer, (ii) provide a clean-cut surface with minimal smearing to facilitate gas flow during reduction experiments, and (iii) obtain samples consistently 3.2 mm in height. Frozen samples were stored under dry ice and transported to the Advanced Photon Source (APS) at Argonne National Laboratory. There, they were placed on top of alumina sample holders (4.5 mm diameter, 10 mm height) within a freeze-drying chamber and maintained under vacuum (~125 mTorr) between -29 and -24 °C for at least 24 h. After complete ice sublimation, the oxide green bodies were ready for reduction and sintering experiments.

2.2. In situ X-ray tomography during reduction and sintering

In situ X-ray tomography was performed at Sector 2-BM at APS. For each experiment, a green body and its alumina holder were carefully removed from the freeze dryer and positioned in the

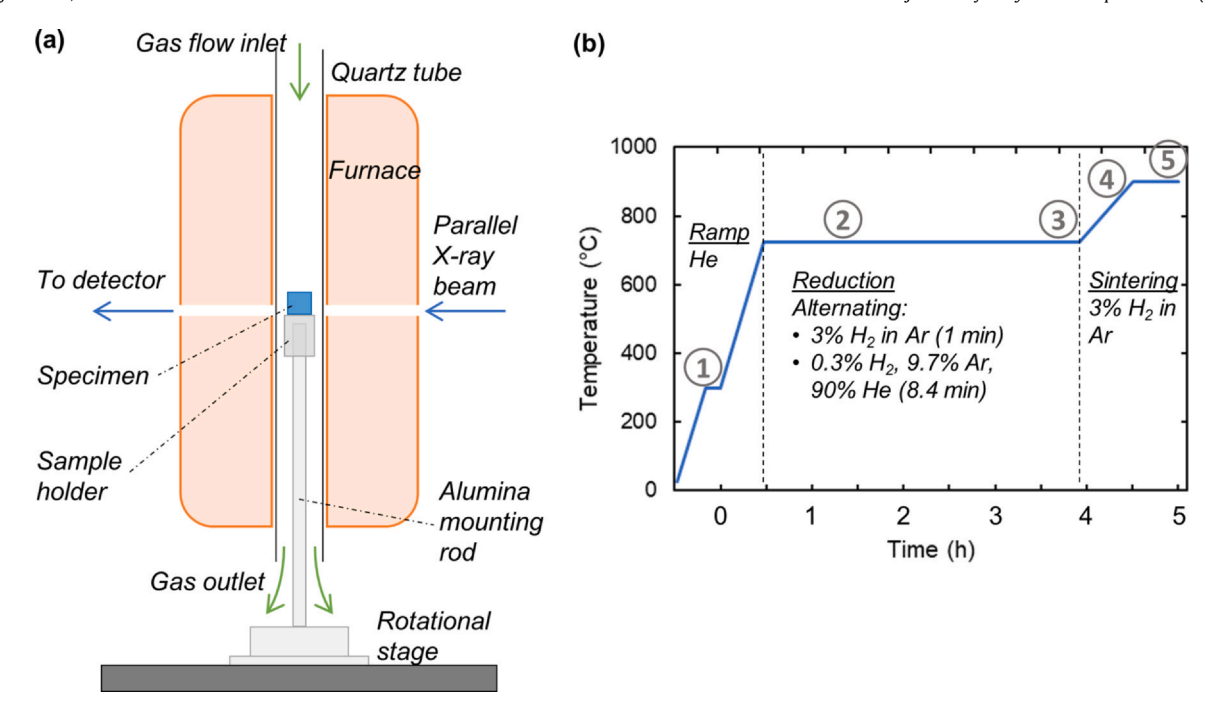


Fig. 1. (a) Schematic of the *in situ* X-ray tomography setup. (b) Temperature and gas program used for the *in situ* reduction and sintering experiments. Circled numbers indicate the time points corresponding to structure snapshots in Figs. 2 and 4.

tomography setup, aligned with the X-ray beam. As illustrated in Fig. 1a. the sample holder was placed on an alumina mounting rod on top of a rotational stage. A custom-built furnace with a quartz tube (~1 mm wall thickness) for gas flow was lowered on top of the sample, and openings on opposites sides of the furnace permitted passage of the X-ray beam. The transmission of monochromatic 40 keV X-rays were detected with a 100 µm thick LuAG scintillator, a 2× objective lens, and a FLIR Oryx camera (ORX-10G-51S5M) that provided a $(1.7 \,\mu\text{m})^3$ voxel size. The resulting field of view was 1.8 mm tall (limited by the X-ray beam size), so the bottom 1.8 mm of the green body was imaged. For a single tomogram, 1500 radiographs were collected at equal rotational increments over the 0-180° range, each with 0.15 s exposure. Each tomogram also included a dark scan (shutter closed) and a blank scan (sample moved out of beam path) to correct camera and beam nonuniformities, respectively. For the blank scan, the sample was moved vertically down out of the field of view. Each tomogram took 6.4 min.

Each experiment started by lowering the furnace, already preheated to 300 °C and with He flowing at 200 sccm, onto the green body. After an initial tomogram, the furnace and green body were heated at 15 °C min⁻¹ to 725 °C, while tomography scans were collected continuously. After equilibrating at 725 °C, the reduction process was started, which consisted of a two-step cycle. First, the reduction gas (3% H₂ in Ar) was flowed at 200 sccm for 1 min. Then, the gas was switched to 180 sccm He + 20 sccm reducing gas, and a tomogram was collected. This two-step cycle was repeated 25 times while holding isothermal at 725 °C. These reduction and scan conditions were chosen based on preliminary testing, which indicated the reduction process during continuous flow of reducing gas was too fast to be resolved: the foam structure deformed too much during a single scan and severe blurring resulted. The alternating reduction gas pulses and tomography scan periods, which we call "quasi in situ," solved this problem. After reduction, the sample was heated at 5 °C min⁻¹ to 900 °C under 200 sccm reducing gas and then sintered for 30 min while tomograms were collected continuously. The complete thermal and gas program is summarized in Fig. 1b.

2.3. Data processing and analysis

Tomographic reconstructions were obtained using the gridrec algorithm [38] in TomoPy [39], and data processing and visualization were performed in Imagel, Matlab (MathWorks), and Amira 6.7.0 (Thermo Scientific) software. To ensure that data analysis was performed on the same region of each foam, even as it shrank and deformed, each tomogram was registered to the previous one by manually identifying the top and bottom slices of a selected subvolume, based on structural pattern recognition. (Rotation and tilt along the vertical axis were negligible). The sub-volume of each foam covered the entire cross-section and between 0.8 and 1.3 mm of green body height. After registration, several structural parameters were calculated from the data to quantify changes during reduction and sintering, as well as to compare foams prepared with different FC suspensions and freezing velocities. All calculations were performed on two-dimensional (2D) cross-section images, or slices, and the three-dimensional (3D) values for each tomogram are reported as the mean ± standard deviation of the 2D measurements.

Foam porosity,

$$p = 1 - (V_s/V_e),$$
 (1)

was calculated from the solid volume, V_s , measured in 2D for every 10th slice, and the envelope volume, V_e , measured every 50th slice. For the solid volume, each slice was first pre-processed by sequentially applying a median filter (radius of 3 pixels), thresholding, applying another median filter (radius of 3 pixels), and removing outliers. This pre-processing sequence was selected as the best of several attempted strategies for reducing noise and artifacts while minimizing alterations to the data. The solid volume was then measured by directly counting solid (i.e., bright) pixels, and the envelope volume was measured by applying a pore filling algorithm [36] to the unfiltered slices and again counting the solid pixels. Changes in the sub-volume height and cross-sectional area were calculated for each time step.

Mean brightness was calculated to track the extent of reduction and sintering, as the brightness of a given voxel is related to the exponential of its electron density (i.e., Beer-Lambert law; equivalently, the natural logarithm of brightness is proportional to electron density). Sintering increases density by eliminating micropores that are smaller or similar in size to the voxel resolution (1.7 µm). Since X-rays are predominantly absorbed by Fe compared to O, mean brightness also increases due to reduction, as the number of Fe atoms per unit volume increases. Mean brightness was calculated for every 10th slice by masking the grayscale image with its thresholded version (used for porosity measurement) – to select only "solid" pixels – and then averaging the brightness of these pixels. For ease of comparison with height and cross-sectional area changes, the inverse of ln(brightness) is reported, which decreases during reduction and sintering [35]. The inverse ln(brightness) values are normalized from 1 to 0, corresponding to the initial (fully Fe₂O₃) and final (fully Fe) scans, respectively.

The distributions of lamellae thickness and pore width were each calculated using the Local Thickness algorithm in ImageJ [40]. This algorithm first identifies one domain in a binary image (e.g., all the pixels of the solid lamellae, or of the pores). Then, for each pixel, Local Thickness is calculated as the diameter of the largest circle (for 2D) or sphere (for 3D) that fits within the domain, thus providing an area-based or volume-based distribution of the feature sizes for that domain. Calculations on 2D images are much faster computationally than 3D, and based on preliminary analyses we determined negligible difference between the two because lamellae/pores are nearly orthogonal to the slices of 3D data. Thus, we calculated Local Thickness on 2D slices throughout the stack of images and used the mean value of 2D measurements to estimate the true (3D) thicknesses.

Lamellae thickness was measured on every 10th slice using the filtered and thresholded images from the porosity measurement, to eliminate small noise. For the pore width measurement, the filtered and thresholded image was first brightness-inverted and masked by the corresponding envelope volume, resulting in a new image with only pores displayed as bright pixels (as required by the Local Thickness algorithm). The pore width distribution was measured from this new image for every 50th slice. The single-slice histograms for lamellae thickness and pore width were summed to obtain cumulative histograms, on which the mean and standard deviation were calculated. The FC wavelength, or the spacing period of parallel lamellae, was calculated as the sum of mean lamellae thickness and mean pore width.

These structural parameters were also measured for the green bodies before reduction and sintering, using a tomogram collected before lowering the furnace onto the sample. Selected reconstructions were rendered in 3D using the thresholded data in Amira software.

3. Results and discussion

3.1. Green body structure

Nearly all FC hard materials – metals and ceramics – are manufactured with a final sintering process step, which is necessary to make the powder-compacted green body mechanically stable. Due to the fragility of green bodies, metallography and imaging are typically done on the sintered foam for structural characterization, but this approach cannot reveal structural changes that occur during the sintering step. X-ray tomography is an ideal probe for imaging fragile green bodies, as it is nondestructive and can provide 3D structural information. Though numerous studies have investigated iron-based FC foams [11,12,14,29,31,32,36,41–43], this is the first, to our knowledge, that relates their green body and reduced-and-sintered structures.

A list of all foams investigated by quasi *in situ* tomography is provided in Table S1 (in the Supplementary Material), including where each foam appears in the figures that follow. The left column

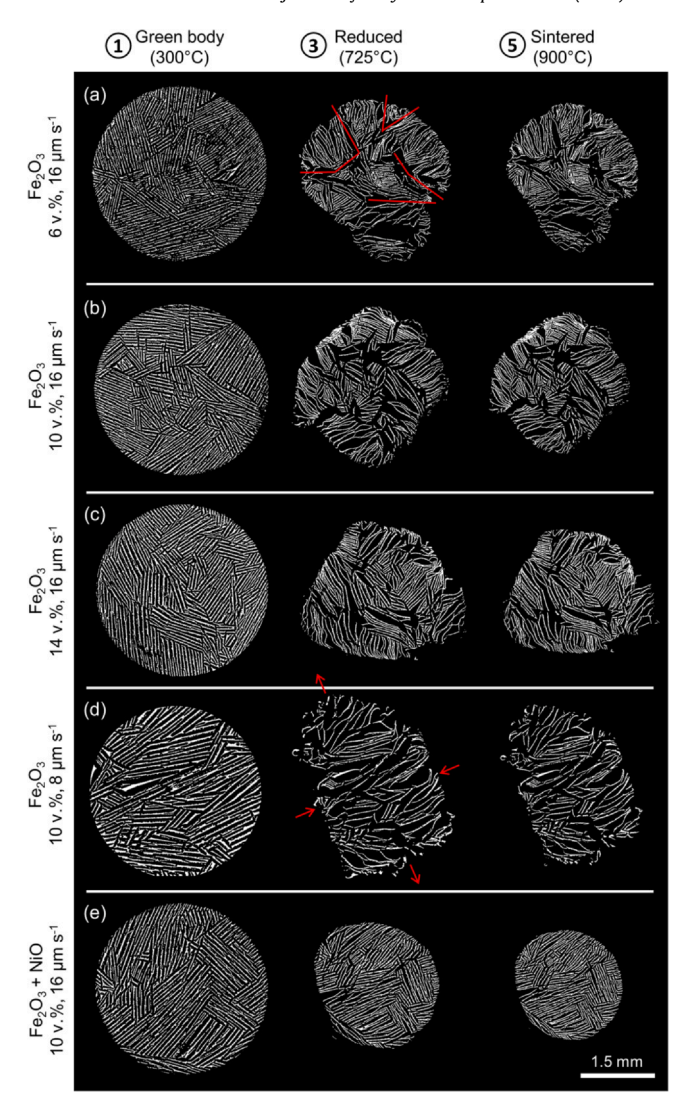


Fig. 2. Cross-sections perpendicular to the freeze-casting direction, taken from X-ray tomography reconstructions. Five foams are shown, each corresponding to a different combination of oxide in the freeze-casting suspension (vol%) and freezing velocity (μ m s⁻¹). Foams cast from (a-d) Fe₂O₃ and (e) Fe₂O₃+NiO powders. Registered cross-sections for each foam are shown for the green body (left), reduced (center), and sintered (right) states, corresponding to circled time markers (1), (3), and (5) in Fig. 1b. Annotations in red are described in the text.

in Fig. 2 shows tomography reconstructed cross-sections (perpendicular to the freezing direction, halfway along the height of the registered volume) for green bodies prepared with various FC suspensions and freezing velocities. The green body structure is typical of water-based directional freeze-casting: lamellae, each extending several mm along the freezing direction, grouped into colonies that contain parallel lamellae, with misalignment between different colonies [31]. Fig. 2a, b, and 2c show three green bodies directionally frozen at a velocity of 16 µm s⁻¹ using suspensions containing 6, 10, and 14 vol% Fe₂O₃, respectively. As the oxide content increases, the cross-sections show an increase in the lamellae thickness and a corresponding decrease in porosity, as expected. Fig. 2b and d show green bodies frozen from a 10 vol% Fe₂O₃ suspension at 16 and $8\,\mu\text{m}\,\text{s}^{-1}$, respectively. The slower freezing in the latter specimen results in a larger spacing period of lamellae - the so-called FC wavelength - as expected.

These trends are summarized quantitatively in Fig. 3. For a fixed freezing velocity $(16 \, \mu m \, s^{-1})$, as the suspension oxide content increases, the FC wavelength does not change (Fig. 3a) and the porosity decreases (Fig. 3b). For a fixed FC suspension (10 vol% oxide), as the

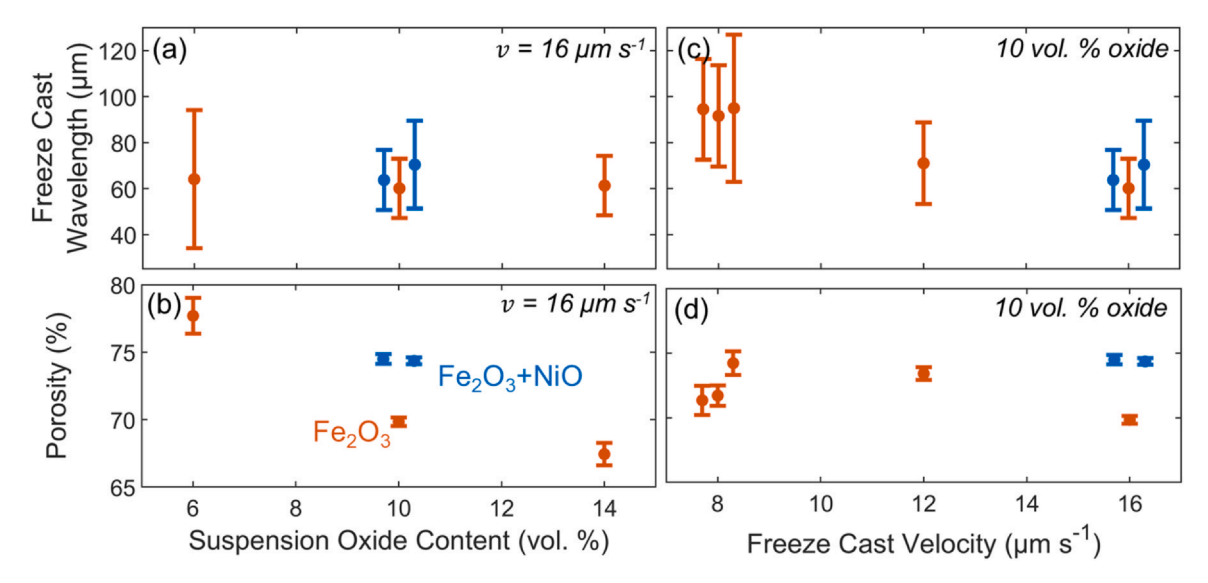


Fig. 3. (a) Freeze-casting wavelength and (b) porosity of green bodies frozen at a velocity of 16 µm s⁻¹, as a function of suspension oxide content. (c) Freeze-casting wavelength and (d) porosity of green bodies prepared from a 10 vol% oxide suspension, as a function of freezing velocity. Each data point represents one green body, and error bars indicate ± the standard deviation of 2D-slice image measurements. Replicate samples are shown slightly displaced along the x-axis for ease of viewing: displacement does not reflect actual changes in oxide content or velocity.

freezing velocity increases, the wavelength decreases (Fig. 3c) and porosity does not change (Fig. 3d). These trends are consistent with standard relationships for FC parameters, in particular $\lambda \sim v^{-n}$, where λ is the FC wavelength, ν is the freezing velocity, and n=1 for submicron powders [20]. For the FC parameters studied here, green body porosity ranged from 67% to 78%, and the mean FC wavelength spanned 60-95 µm. As described in the Experimental procedures, the FC wavelength was calculated for several 2D slices in the 3D tomography volume and then averaged. The standard deviation of these measurements (Fig. 3 error bars) was quite large for FC wavelength, indicating a large variation in lamellae thickness and pore width. Based on inspection of the cross-sections and their 2D thickness histograms, the lamellae structure is quite consistent from top-to-bottom through the foam, which justifies the 2D measurement approach to obtain 3D values (i.e., the cross-section at any given height is structurally representative). Rather, the variation in lamellae thickness and pore width is present in each individual cross-section; for example, for a Fe₂O₃ green body freeze-cast at 8 µm s⁻¹ from a suspension with 10 vol% oxide, the 3D standard deviation for pore width is 11.2 um and the standard deviations of individual 2D slices range from 10.7 to 11.5 µm.

For two of the FC conditions – 10 vol% oxide with 8 or $16 \,\mu\text{m s}^{-1}$ replicate green bodies were tested. As shown in Fig. 3c, for either group of replicates, the mean wavelength values are well within the single-sample error bars, indicating that the FC procedure was reproducible for a given set of FC parameters. The porosities of replicate Fe₂O₃ green bodies (Fig. 3d, $8 \,\mu\text{m s}^{-1}$) are fairly reproducible, and the Fe₂O₃+NiO green bodies (Fig. 3d, $16 \,\mu\text{m s}^{-1}$) had ~4% higher porosity than their analog Fe₂O₃ green bodies.

3.2. Structural evolution during reduction and sintering

All green bodies exhibited similar behavior during reduction and sintering, as shown by cross-sections in the cast, reduced, and sintered states in Fig. 2. Green body structure did not change appreciably during the initial heating from 300 to 725 °C (not shown). Upon reduction, the foams distorted and shrank macroscopically due to the molar volume shrinkage from Fe₂O₃ to Fe; subsequent sintering (heating from 725 to 900 °C and holding isothermally) led to further shrinkage due to densification of Fe within individual lamellae.

The most notable structural changes are the buckling of lamellae, leading to substantial anisotropy in the macroscopic shrinkage. For example, in Fig. 2d, the lamellae are mostly aligned left-to-right in the cross-section image of the green body, and they contract predominantly along this orientation as they fan apart in the perpendicular direction (annotated with red arrows). This buckling behavior is more fully evident in the time lapse of the cross-section (Video S1 in the Supplementary Material) and 3D renderings (Fig. 4, left column, and Video S2). Buckling is a common deformation mode for ice-templated FC foams, particularly during mechanical compression testing [44,45]. Here, however, the mechanical stress is not applied externally, but rather it arises internally from the reduction volume change. A mismatch in the reduction rate at different locations (e.g., from the outer-to-inner regions of the foam) causes different contraction rates, and the resulting stresses deflect the high aspect ratio lamellae in the direction perpendicular to their plane [32]. The buckling of aligned lamellae also leads to separation at the boundaries between misaligned colonies of lamellae (Fig. 2a, red lines).

Buckling was more severe for foams that started with more highly aligned lamellae. For example, the green bodies in Fig. 2a-c each begin with several colonies of lamellae, and they exhibit comparable buckling behavior (the time lapse of Fig. 2b is provided in Video S3, with 3D renderings in Fig. 4, center column, and Video S4), while the green body in Fig. 2d begins with most lamellae aligned in a single colony, and the buckling effect is much more pronounced. Larger green bodies (~1 cm diameter) typically do not exhibit buckling during reduction and sintering [11], suggesting that a higher number of misaligned colonies helps prevent buckling. Once several dozen colonies are present, such as in the larger foams, the shrinkage behavior is much more isotropic, reflective of the orientationally-averaged structure in the cross-section. For some applications, highly aligned lamellae are desirable and can be achieved using nucleation control features in the freeze-casting mold [46]. However, for creating metal foams by reducing and sintering FC oxide green bodies, such highly-aligned structures are susceptible to distortion and thus the fabrication process is likely to be poorly reproducible.

The Fe_2O_3+NiO green body (cross-section in Fig. 2e and Video S5; 3D rendering in Fig. 4, right column, and Video S6) exhibited much more isotropic shrinkage without buckling, as compared to all the

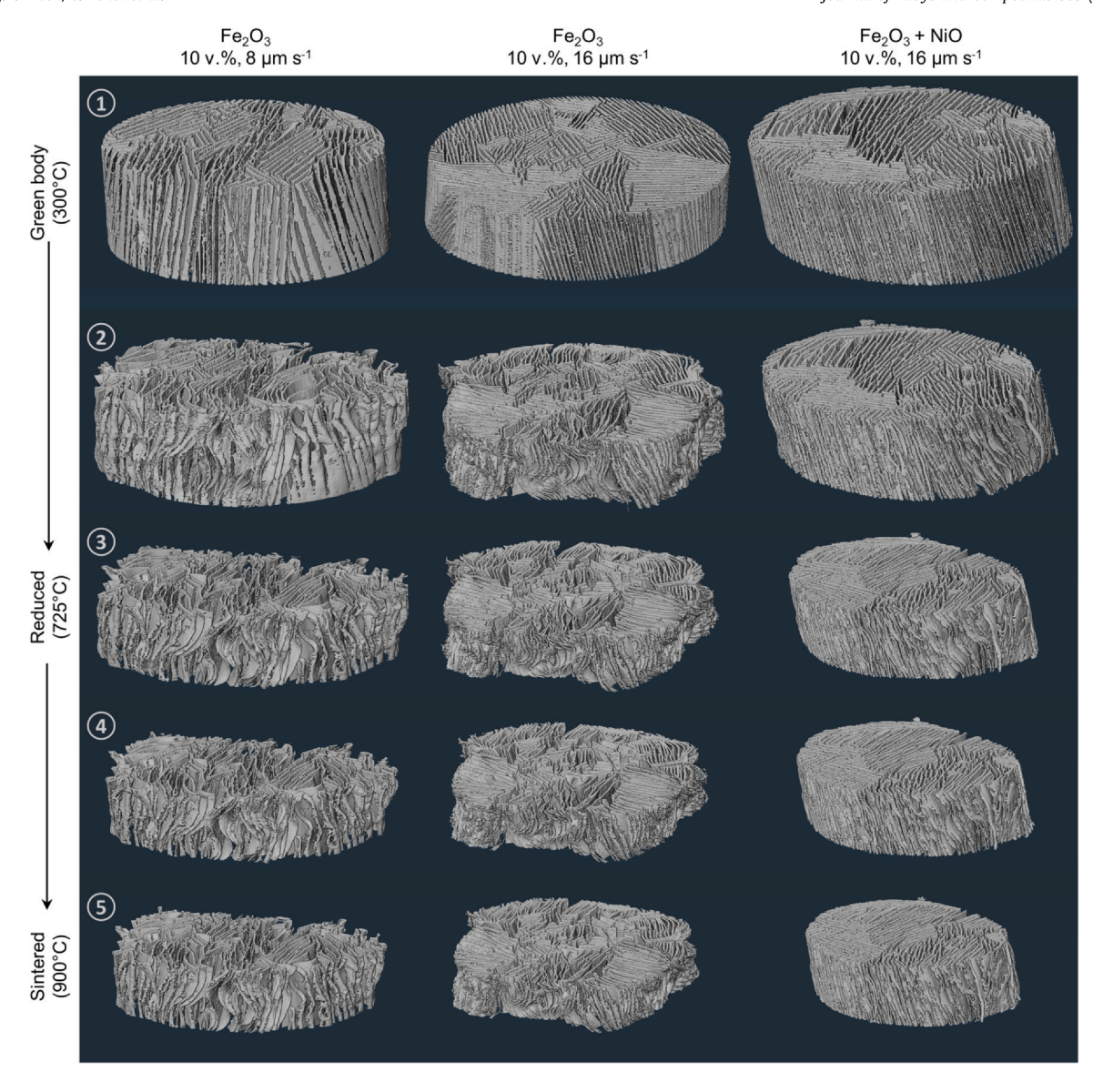


Fig. 4. 3D structural evolution of sub-volumes for three foams (two cast from Fe_2O_3 and one from Fe_2O_3 +NiO powder suspensions) prepared with different freeze-casting parameters: oxide content in suspension (v.%) and freezing velocity (μ m s⁻¹). The samples shown here left-to-right correspond to Fig. 2d, b, and e. Images arranged vertically correspond to the circled time markers (1)-(5) shown in Fig. 1b. Green bodies shown here are approximately 3.6 mm in diameter and 0.84–1.30 mm tall.

 Fe_2O_3 green bodies. This unique structural evolution is likely caused by the much faster reduction kinetics for NiO compared to Fe_2O_3 [11,35,47], such that NiO is quickly reduced throughout the foam and then provides catalytic sites for further Fe_2O_3 reduction uniformly throughout the foam volume. In contrast, the NiO-free Fe_2O_3 green bodies have a distinct spatial progression of reaction outside-inward (Videos S1 and S3), leading to the mismatch stresses that cause buckling and anisotropic shrinkage.

3.3. Quantitative structural parameters

The foam structural evolution is quantified using several parameters, provided in Fig. 5 for the three exemplary foams depicted in Fig. 2b, d, e and Fig. 4. Our heating program and gas environment (Fig. 1b) were chosen so as to examine separately the effects of reduction and sintering, which occur simultaneously for typical heating and reduction processes [35]. The extents of reduction and sintering are assessed using the normalized inverse ln(brightness) of the solid voxels versus time, measured from tomographic reconstructions (Fig. 5a). The natural logarithm of voxel brightness is

proportional to the X-ray absorption, which increases with electron density. Here, the inverse brightness is used for ease of visual comparison with the macroscopic shrinkage (Fig. 5b-c). As shown in Fig. 5a, the inverse ln(brightness) decreases during reduction, due to the higher electron density in Fe vs. Fe₂O₃, and decreases further during sintering, as the intra-lamellar microporosity is eliminated [32]. The micropores within lamellae are under 1 µm in diameter, i.e., smaller than the 1.7 µm voxel dimension, so they are not spatially resolved but instead affect the measured voxel brightness. The gently sloping plateau in Fig. 5a at the end of the reduction step indicates that reduction was nearly fully complete before sintering began, so the effects of reduction and sintering on structural evolution can be mostly distinguished for analysis. Some sintering likely occurs during the reduction at 725 °C, but only at a negligible rate compared to the sintering step at 900 °C. The Fe₂O₃+NiO foam (Fig. 5, blue data markers) was reduced faster than the pure Fe₂O₃ foams, as discussed earlier.

Macroscopic shrinkage is reported in Fig. 5b-c as the foam height and cross-sectional area, each normalized to their initial values. All foams exhibit 30% shrinkage along their height during reduction,

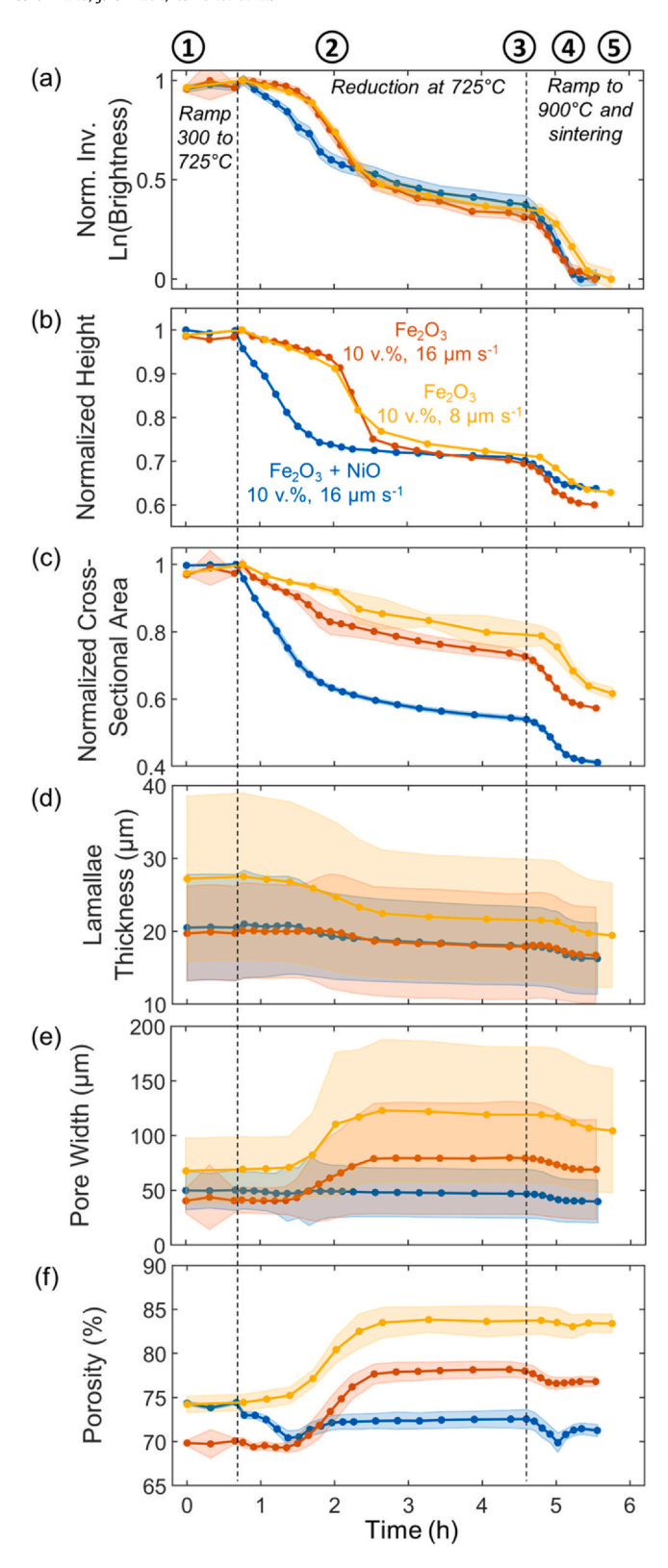


Fig. 5. Evolution of structural characteristics of the three foams shown in Fig. 4, during the thermal and gas treatment shown in Fig. 1b. Each point represents an individual tomography reconstruction; solid lines are to guide the eye. Shading represents ± standard deviations of 2D-slice image measurements. Circled time markers (1)-(5) correspond with Figs. 1b, 2, and 4.

with an additional 5–10% shrinkage during sintering. Again, the faster reduction kinetics for the Fe_2O_3 +NiO foam are evident. Cross-sectional shrinkage varies between foams: Fe_2O_3 foams (Fig. 5,

vellow and orange data markers) exhibit 21-27% reduction shrinkage with additional 16-17% sintering shrinkage, while the Fe₂O₃+NiO foam shrinks 47% and then 11%. The smaller cross-sectional shrinkage of pure Fe₂O₃ foams is a result of the lamellae buckling (e.g., Fig. 2b, d vs. Fig. 2e), which has the effect of enlarging the crosssection, somewhat counteracting the reduction and sintering shrinkage. By multiplying the normalized height and cross-sectional area for each foam, the relative contributions of reduction and sintering to the total volumetric shrinkage can be calculated: reduction accounted for 73-75% of total shrinkage in the Fe₂O₃ foams and 86% of total shrinkage in the Fe₂O₃+NiO foam. The larger contribution from reduction for the Fe₂O₃+NiO foam cannot be explained by molar volume changes, since shrinkage due to molar volume is smaller for NiO/Ni (Ni molar volume in NiO/Ni = 1.70/1) than for Fe_2O_3/Fe (Fe molar volume = 2.14/1). Rather, the most likely explanation is the buckling effect, which is more prominent during reduction of the Fe₂O₃ foams. It is also possible that more sintering occurs at 725 °C in the Fe₂O₃+NiO foam compared to the Fe₂O₃ foam, due to the smaller powder size of NiO vs. Fe₂O₃.

In a similar study, Lichtner et al. [33] investigated the sintering behavior (without reduction) of directionally freeze-cast, lamellar green bodies composed of 40:60 vol% lanthanum strontium manganite (1 µm powder) and yttria-stabilized zirconia (0.5 µm). Using optical dilatometry during heating to 1400 °C, they observed linear shrinkage of 16% and 19% in the directions parallel and perpendicular to freezing, respectively. These values are larger than the sintering contribution observed here in Fe₂O₃ and Fe₂O₃+NiO foams (linear shrinkage of 5-10% parallel and 8-10% perpendicular to freezing, calculated from cross-sectional shrinkage), though direct comparison is difficult given the preceding reduction process. The cross-sectional shrinkage for combined reduction and sintering (Fig. 5c) corresponds to radial shrinkage of 21-36%, which is much smaller than the combined height shrinkage of 35-40%. Thus, the anisotropic trend observed here for reduction and sintering – greater shrinkage along the freeze-casting direction - is in agreement with the study by Lichtner et al. on sintering alone. As described there, the anisotropic trend can be explained by a higher density of interparticle contacts along the freeze-casting direction, since the pores act as gaps in the particle network in the direction perpendicular to freezing. The 35-40% combined height shrinkage observed here is in excellent agreement with work by Kenel et al. using interrupted Xray tomography to measure linear shrinkage of extrusion-printed Fe-20Ni-5Mo microfilaments (330 µm initial diameter) during reduction and sintering of a blend of binary oxide precursors [35].

Throughout reduction and sintering, the lamellae thickness (Fig. 5d) and pore width (Fig. 5e) exhibit very broad distributions about their mean values, as also observed for the green bodies (Fig. 3a, c) and explained earlier. Mean lamellae thickness decreases from 20 to $16 \,\mu m$ in foams freeze-cast at $16 \,\mu m \, s^{-1}$ and from 27 to $19 \,\mu m$ in the Fe₂O₃ foam frozen at $8 \,\mu m \, s^{-1}$. For the Fe₂O₃ foams, mean pore width is initially larger for the foam freeze-cast at a velocity of 8 vs. 16 µm s⁻¹ (Fig. 5e, yellow vs. orange). For the former velocity, pore width increases from 70 to 110 µm during reduction, followed by a slight decrease to 103 µm upon sintering. Mean pore width for the 16 μm s⁻¹ velocity shows a similar trend, changing from 42 to 77 to $68 \, \mu m$. These foams' increase in pore width during reduction is again explained by the buckling of lamellae, which increases pore width despite the overall macroscopic shrinkage; thereafter, the pores shrink slightly during sintering when no further buckling is observed. The Fe₂O₃+NiO foam (Fig. 5e, blue) exhibits less pronounced changes in pore width, consistent with the absence of buckling, with pore width shrinking from 50 to 48 µm during reduction and then to 42 µm after sintering.

The porosity of the Fe_2O_3 and Fe_2O_3+NiO foams (Fig. 5f) are initially similar, 70–75%, since they were all freeze-cast from suspensions containing 10 vol% oxide powder. The porosities of the Fe_2O_3

foams increase by 8-9% during reduction and decrease slightly during sintering, while the Fe₂O₃+NiO foam decreases in porosity by 2% in reduction and another 2% during sintering. The evolution of foam porosity is affected by competing factors: the reduction shrinkage decreases the solid volume, thus increasing porosity, while the macroscopic shrinkage decreases the envelope volume of the foam, thus decreasing the porosity. For reduction of the Fe₂O₃ foams (Fig. 5f, yellow and orange), the buckling effect partially counteracts the envelope volume shrinkage, such that the solid volume decrease is the prevailing factor and the porosity increases. Without the buckling, the Fe₂O₃+NiO foam exhibits only minor porosity changes, suggesting that the macroscopic shrinkage and solid volume shrinkage occur proportionally. The final 71% porosity of the Fe₂O₃+NiO foam is also in fair agreement with prior work on larger Fe-20Ni foams (~1 cm in diameter and height) processed under similar conditions (62–67% porous) [11].

While the FC parameters (suspension oxide content and freezing velocity) have a clear effect on green body structure (Fig. 3), structural evolution during reduction and sintering is similar across Fe_2O_3 foams regardless of their FC parameters (Fig. 5, yellow and orange). Tests on three replicate foams freeze-cast at $8\,\mu m\,s^{-1}$ from a suspension containing $10\,vol\%$ Fe_2O_3 also show similar structural changes (Fig. S1), which indicates that the reduction and sintering process is quite reproducible and that the quasi in situ tomography method provides reliable measurement. Ultimately, the lamellae colony structure and presence of NiO are the predominant factors influencing structural evolution via changes to lamellae buckling, reduction kinetics, and (an)isotropic shrinkage.

While all foams are structurally stable after reduction and sintering, the lamellae buckling and shrinkage behavior will affect mechanical properties of the resulting foams. Fortunately, larger foams (~1 cm diameter) generally have not exhibited such pronounced buckling [11].

4. Conclusions

High-temperature reduction and sintering of oxide-powder green bodies created by freeze-casting is a versatile process route for manufacturing metallic foams, with a wide array of compositions and applications. The evolution of foam structure – from oxide green body, to reduced metallic state, to sintered state – is revealed here using quasi *in situ* X-ray microtomography, enabling separate analysis of the reduction and sintering steps. Foams were directionally freeze-cast, using suspensions with two oxide particle compositions (Fe₂O₃ and Fe₂O₃+NiO) solidified at various velocities, to obtain green bodies of differing initial porosity and pore size. Macroscopic shrinkage and changes to lamellae thickness, pore width, and total porosity were quantified from the tomography reconstructions.

Green body structures followed typical FC trends: porosity increased with lower oxide powder content in the FC suspension, and pore width decreased with higher freezing velocities. Upon reduction to metal, the lamellae in Fe foams buckle substantially in response to mismatch stresses induced by spatially-varying reduction shrinkage rates. Buckling is most severe when lamellae are highly aligned. Fe-20Ni foams, in contrast, do not exhibit buckling, likely due to the faster reduction kinetics of Ni/NiO that facilitate more uniform shrinkage rates throughout the foam volume. Macroscopic shrinkage is anisotropic, with greater shrinkage along the FC direction than perpendicular to it, in agreement with prior work on the sintering process alone. The oxide reduction step is the dominant contribution to foam shrinkage: 73–86% of total volume shrinkage.

CRediT authorship contribution statement

S. K. Wilke: conceptualization, methodology, investigation, formal analysis, writing – original draft, review & editing. **J. B. Mack**:

methodology, investigation, formal analysis, writing – original draft, review & editing. **C. Kenel**: investigation, visualization, writing – review & editing. **D. C. Dunand**: conceptualization, formal analysis, writing – review & editing, funding acquisition.

Declaration of Competing Interest

David Dunand discloses a financial interest in Cell Mobility, Inc., a company involved with metal foams.

Acknowledgments

This work was supported by the National Science Foundation (NSF CMMI-1562941). Experiments and characterization made use of the Materials Characterization and Imaging Facility, the NUANCE Center (supported by SHyNE under NSF ECCS-1542205, MRSEC under NSF DMR-1720139, the International Institute for Nanotechnology, the Keck Foundation, and the State of Illinois), and the Center for Advanced Molecular Imaging (NCI CCSG P30 CA060553) at Northwestern University (NU). Tomography experiments were performed at Sector 2-BM of the Advanced Photon Source (APS), operated by Argonne National Laboratory (DOE DE-AC02-06CH11357). The authors gratefully acknowledge Mr. Pavel Shevchenko (APS) and Ms. Kristen Scotti (NU) for their help in collecting tomography data and for insightful discussions.

Appendix A. Supporting information

Supplementary Material including videos associated with this article can be found in the online version at doi:10.1016/j.jallcom. 2021.161707.

References

- [1] R. Singh, P.D. Lee, R.J. Dashwood, T.C. Lindley, Titanium foams for biomedical applications: a review, Mater. Technol. 25 (2010) 127–136.
- [2] M. Guden, E. Celik, S. Cetiner, A. Aydin, Metals foams for biomedical applications: processing and mechanical properties, in: N. Hasirci, V. Hasirci (Eds.), Biomaterials. Advances in Experimental Medicine and Biology, Springer, Boston, MA. 2004, pp. 257–266.
- [3] N. Kleger, M. Cihova, K. Masania, A.R. Studart, J.F. Löffler, 3D printing of salt as a template for magnesium with structured porosity, Adv. Mater. 31 (2019) 1903783.
- [4] C.-L. Myung, J. Kim, W. Jang, D. Jin, S. Park, J. Lee, Nanoparticle filtration characteristics of advanced metal foam media for a spark ignition direct injection engine in steady engine operating conditions and vehicle test modes, Energies 8 (2015) 1865–1881.
- [5] J. Rösler, O. Näth, S. Jäger, F. Schmitz, D. Mukherji, Fabrication of nanoporous Nibased superalloy membranes, Acta Mater. 53 (2005) 1397–1406.
- [6] J. Liang, C.D. Christiansen, K. Engelbrecht, K.K. Nielsen, R. Bjørk, C.R.H. Bahl, Characterization of freeze-cast micro-channel monoliths as active and passive regenerators, Front. Energy Res. 8 (2020).
- [7] J. Liang, C.D. Christiansen, K. Engelbrecht, K.K. Nielsen, R. Bjørk, C.R.H. Bahl, Heat transfer and flow resistance analysis of a novel freeze-cast regenerator, Int. J. Heat Mass Transf. 155 (2020) 119772.
- [8] G. Han, J.H. Um, H. Park, K. Hong, W.-S. Yoon, H. Choe, Hierarchically structured nanoporous copper for use as lithium-ion battery anode, Scr. Mater. 163 (2019) 9–13
- [9] H. Yu, C. HQ, P. MQ, Y. Tang, K. Zeng, F. Peng, W. HJ, Effect of the metal foam materials on the performance of methanol steam micro-reformer for fuel cells, Appl. Catal. A Gen. 327 (2007) 106–113.
- [10] K.L. Scotti, D.C. Dunand, Freeze Casting A review of processing, microstructure and properties via the open data repository, FreezeCasting.net, Prog. Mater. Sci. 94 (2018) 243–305.
- [11] S.K. Wilke, D.C. Dunand, Fe-Ni foams self-heal during redox cycling via reversible formation/homogenization of a ductile Ni scaffold, J. Mater. Chem. A 8 (2020) 19375–19386.
- [12] J.S. Kang, Y. Noh, J.J.-Y. Kim, H. Choi, T.H. Jeon, D. Ahn, J.J.-Y. Kim, S.-H. Yu, H. Park, J.-H. Yum, W. Choi, D.C. Dunand, H. Choe, Y. Sung, Iron oxide photoelectrode with multidimensional architecture for highly efficient photoelectrochemical water splitting. Angew. Chem. Int. Ed. 56 (2017) 6583–6588.
- [13] S. Deville, Freezing Colloids: Observations, Principles, Control, and Use, Springer, Cham. Switzerland. 2017.

- [14] T. Um, S.K. Wilke, H. Choe, D.C. Dunand, Effects of pore morphology on the cyclical oxidation/reduction of iron foams created via camphene-based freeze casting, J. Alloy. Compd. 845 (2020) 156278.
- [15] H.J. Choi, T.Y. Yang, S.Y. Yoon, B.K. Kim, H.C. Park, Porous alumina/zirconia layered composites with unidirectional pore channels processed using a tertiary-butyl alcohol-based freeze casting, Mater. Chem. Phys. 133 (2012) 16–20.
- [16] B. Delattre, H. Bai, R.O. Ritchie, J. De Coninck, A.P. Tomsia, Unidirectional freezing of ceramic suspensions: in situ x-ray investigation of the effects of additives, ACS Appl. Mater. Interfaces 6 (2014) 159–166.
- [17] J. Zou, Y. Zhang, R. Li, Effect of suspension state on the pore structure of freezecast ceramics, Int. J. Appl. Ceram. Technol. 8 (2011) 482–489.
- [18] D. Ghosh, H. Kang, M. Banda, V. Kamaha, Influence of anisotropic grains (platelets) on the microstructure and uniaxial compressive response of ice-templated sintered alumina scaffolds, Acta Mater. 125 (2017) 1–14.
- [19] D. Ghosh, N. Dhavale, M. Banda, H. Kang, A comparison of microstructure and uniaxial compressive response of ice-templated alumina scaffolds fabricated from two different particle sizes, Ceram. Int. 42 (2016) 16138–16147.
- [20] S. Deville, E. Saiz, A.P. Tomsia, Ice-templated porous alumina structures, Acta Mater. 55 (2007) 1965–1974.
- [21] Y. Chino, D.C. Dunand, Directionally freeze-cast titanium foam with aligned, elongated pores, Acta Mater. 56 (2008) 105–113.
- [22] G.J. Gouws, N. Shortt, Microstructured silver surfaces produced by freeze casting for enhanced phase change heat transfer, J. Phys. Conf. Ser. 660 (2015) 012045.
- [23] D. Driscoll, A.J. Weisenstein, S.W. Sofie, Electrical and flexural anisotropy in freeze tape cast stainless steel porous substrates, Mater. Lett. 65 (2011)
- [24] A.I.C. Ramos, D.C. Dunand, Preparation and characterization of directionally freeze-cast copper foams, Metals 2 (2012) 265–273.
- [25] H. Park, M. Choi, H. Choe, D.C. Dunand, Microstructure and compressive behavior of ice-templated copper foams with directional, lamellar pores, Mater. Sci. Eng. A 679 (2017) 435–445.
- [26] H. Jo, M.J. Kim, H. Choi, Y.-E. Sung, H. Choe, D.C. Dunand, Morphological study of directionally freeze-cast nickel foams, Metall. Mater. Trans. E 3 (2016) 46–54.
- [27] H. Park, H.-H. Cho, K. Kim, K. Hong, J.-H. Kim, H. Choe, D.C. Dunand, Surface-oxidized, freeze-cast cobalt foams: microstructure, mechanical properties and electrochemical performance, Acta Mater. 142 (2018) 213–225.
- [28] A. Röthlisberger, S. Häberli, R. Spolenak, D.C. Dunand, Synthesis, structure and mechanical properties of ice-templated tungsten foams, J. Mater. Res. 31 (2016) 753–764.
- [29] A.A. Plunk, D.C. Dunand, Iron foams created by directional freeze casting of iron oxide, reduction and sintering, Mater. Lett. 191 (2017) 112–115.
- [30] K. Nam, S. Lee, K. Hong, J.S. Kang, H. Jo, H. Park, Y.-E. Sung, P. Jenei, J. Gubicza, K. Kwon, H.-S. Nam, H. Choe, Freeze casting is a facile method to create solid solution alloy foams: Cu-Ni alloy foams via freeze casting, Adv. Eng. Mater. 21 (2019) 1801265.
- [31] S.K. Wilke, D.C. Dunand, Structural evolution of directionally freeze-cast iron foams during oxidation/reduction cycles, Acta Mater. 162 (2019) 90–102.

- [32] S.K. Wilke, R.A. Lundberg, D.C. Dunand, Hierarchical structural changes during redox cycling of Fe-based lamellar foams containing YSZ, CeO2, or ZrO2, ACS Appl. Mater. Interfaces 12 (2020) 27190–27201.
- [33] A. Lichtner, D. Roussel, D. Röhrens, D. Jauffres, J. Villanova, C.L. Martin, R.K. Bordia, Anisotropic sintering behavior of freeze-cast ceramics by optical dilatometry and discrete-element simulations. Acta Mater. 155 (2018) 343–349.
- [34] B. Hugonnet, J.M. Missiaen, C.L. Martin, C. Rado, Effect of contact alignment on shrinkage anisotropy during sintering: stereological model, discrete element model and experiments on NdFeB compacts, Mater. Des. 191 (2020) 108575.
- [35] C. Kenel, T. Davenport, X. Li, R.N. Shah, D.C. Dunand, Kinetics of alloy formation and densification in Fe-Ni-Mo microfilaments extruded from oxide- or metalpowder inks, Acta Mater. 193 (2020) 51–60.
- [36] S.K. Wilke, D.C. Dunand, In operando tomography reveals degradation mechanisms in lamellar iron foams during redox cycling at 800 °C, J. Power Sources 448 (2020) 227463.
- [37] C. Stolze, T. Janoschka, U.S. Schubert, F.A. Müller, S. Flauder, Directional solidification with constant ice front velocity in the ice-templating process, Adv. Eng. Mater. 18 (2016) 111–120.
- [38] F. Marone, M. Stampanoni, Regridding reconstruction algorithm for real-time tomographic imaging, J. Synchrotron Radiat. 19 (2012) 1029–1037.
- [39] D. Gürsoy, F. De Carlo, X. Xiao, C. Jacobsen, TomoPy: a framework for the analysis of synchrotron tomographic data, J. Synchrotron Radiat. 21 (2014) 1188–1193.
- [40] R.P. Dougherty, K.-H. Kunzelmann, Computing local thickness of 3D structures with ImageJ, Microsc. Microanal. 13 (2007) 1678–1679.
- [41] R. Sepúlveda, A.A. Plunk, D.C. Dunand, Microstructure of Fe2O3 scaffolds created by freeze-casting and sintering, Mater. Lett. 142 (2015) 56-59.
- [42] H. Park, T. Um, K. Hong, J.S. Kang, H.-S. Nam, K. Kwon, Y.-E. Sung, H. Choe, Effects of powder carrier on the morphology and compressive strength of iron foams: water vs camphene, Metall. Mater. Trans. B 49 (2018) 2182–2190.
- [43] P.J. Lloreda-Jurado, E.M. Pérez-Soriano, A. Paúl, J. Herguido, J.A. Peña, R. Sepúlveda, Doped iron oxide scaffolds with gradient porosity fabricated by freeze casting: pore morphology prediction and processing parameters, Mater. Sci. Technol. 36 (2020) 1227–1237.
- [44] M.M. Porter, R. Imperio, M. Wen, M.A. Meyers, J. McKittrick, Bioinspired scaffolds with varying pore architectures and mechanical properties, Adv. Funct. Mater. 24 (2014) 1978–1987.
- [45] A. Ojúva, M. Järveläinen, M. Bauer, L. Keskinen, M. Valkonen, F. Akhtar, E. Levänen, L. Bergström, Mechanical performance and CO₂ uptake of ion-exchanged zeolite A structured by freeze-casting, J. Eur. Ceram. Soc. 35 (2015) 2607–2618.
- [46] H. Bai, Y. Chen, B. Delattre, A.P. Tomsia, R.O. Ritchie, Bioinspired large-scale aligned porous materials assembled with dual temperature gradients, Sci. Adv. 1 (2015) 1500849.
- [47] Q. Jeangros, T.W. Hansen, J.B. Wagner, C.D. Damsgaard, R.E. Dunin-Borkowski, C. Hébert, J. Van Herle, A. Hessler-Wyser, Reduction of nickel oxide particles by hydrogen studied in an environmental TEM, J. Mater. Sci. 48 (2013) 2893–2907.